Na co-cations promoted stability and activity of Pd/SSZ-13 for low-temperature NO adsorption

Dan Li [a], Guoju Yang [b], Mengyang Chen [b], Lei Pang [c], Yanbing Guo [d], Jihong Yu [b,e,*], Tao Li [a,**]

[a] *Key Laboratory of Material Chemistry for Energy Conversion and Storage (Ministry of Education), Hubei Key Laboratory of Material Chemistry and Service Failure, School of Chemistry and Chemical Engineering, Huazhong University of Science and Technology, Wuhan 430074, China*
[b] *State Key Laboratory of Inorganic Synthesis and Preparative Chemistry, College of. Chemistry, Jilin University, Changchun 130012, China*
[c] *Dongfeng Trucks R&D Center, Wuhan 430056, China*
[d] *Key Laboratory of Pesticide & Chemical Biology of Ministry of Education, Institute of Environmental and Applied Chemistry, College of Chemistry, Central China Normal University, Wuhan 430079, China*
[e] *International Center of Future Science, Jilin University, Changchun 130012, China*

ARTICLE INFO

ABSTRACT

The abatement of harmful nitrogen oxides (NO_x) emission during vehicle cold start is challenging. Passive NO_x adsorbers (PNAs) have proven to effectively alleviate NO_x emission at low temperatures. In this work, Pd-based Na-SSZ-13 (Pd/Na-13) was synthesized and hydrothermally aged to investigate the effect of Na co-cations on the structure and activity of Pd/SSZ-13 for low-temperature NO adsorption. Compared to Pd-based NH_4-SSZ-13 (Pd/NH_4-13), Pd/Na-13 exhibited superior stability and activity promoted by Na co-cations in SSZ-13. DRIFTS and ^{27}Al MAS NMR demonstrated that Na co-cations protected Si-O(H)-Al bonds and thus helping to mitigate dealumination during hydrothermal aging. NO- and CO-DRIFTS studies proved that Pd^{2+} sites existed in aged Pd/Na-13 dominantly. Strikingly, the aged Pd/Na-13 exhibited excellent adsorption capacity with additional NO adsorption at above 100 °C. Our work reveals the co-cation effects on the local environments of Pd/SSZ-13, expecting to provide guidance on the catalyst modification or optimization for low-temperature NO adsorption.

1. Introduction

Regulations on vehicle emissions are increasingly stringent, it is impending to reduce the emission of nitrogen oxides (NO_x) from lean-burn engines [1,2]. Up to now, selective catalytic reduction (SCR) is considered as the most efficient system with NO_x conversion close to 100% at a temperature above 200 °C [3–5]. However, most of NO_x is emitted during vehicle operation at a temperature below 200 °C (i.e., cold-start period) [6]. To reduce the NO_x emission during the cold-start period, passive NO_x adsorber (PNA) is put forward and collocated with the SCR catalyst [7,8]. In the cooperation, the PNA can trap NO_x at the temperatures below 200 °C and desorb the NO_x when the SCR catalyst is aroused to work in high efficiency [9,10].

The application of PNA to remove NO_x through combining three-way catalysts was first reported by Cole et al. [11]. Till now, researchers have made great efforts to improve the performance of PNA materials from metal-supported oxides to metal-modified zeolites [12,13]. It was found early that metal-supported oxides showed excellent NO_x adsorption performance. For example, Ji et al. [14] reported the great potential of γ-Al_2O_3 supported Pt for low-temperature PNA applications. Subsequently, Pt- and Pd-promoted CeO_2-ZrO_2 mixed oxides were applied in the vehicle cold-start period successfully by Ji's team [15]. Chen et al. [16] found that zeolites-supported Pd (Pd/zeolites) showed superior NO storage capacity. Compared with CeO_2-based adsorber, Pd/zeolites possess superb resistance to sulfur and hydrocarbon poisoning. Noticeably, the PNA performance of Pd/zeolite materials was closely related to the framework structure of zeolite (i.e., SSZ-13, ZSM-5, or BEA). Afterward, some comparative studies in terms of different framework structures and hydrothermal aging treatment were reported. For instance, Lee et al. [17] reported that zeolites with small pore size can restrict Pd mobility, thereby preventing the formation of bulk PdO during hydrothermal aging treatment. Khivantsev et al. [18] highlighted that

---

Pd/SSZ-13 showed the highest hydrothermal stability among the Pd/SSZ-13, Pd/ZSM-5, and Pd/BEA with similar Si/Al ratios.

Indeed, hydrothermal stability is one of the key factors to evaluate the efficacy and application of PNA, especially for post-treatment catalysts. As proposed by Gu et al. [9], PNA should possess resistance to severe thermal aging and poisoning. In previous studies of PNA, hydrothermal aging was initially proposed to activate Pd/SSZ-13 by Ryou et al. [19]. Shan's group [20] found a slight increase in PNA performance after hydrothermal aging under mild conditions. While severe hydrothermal aging could cause structural changes for Pd/SSZ-13, thereby resulting in its inevitable deactivation. Recently, Zhao et al. [21] systematically investigated the deactivation of Pd/SSZ-13 by hydrothermal aging for PNA application. They found that both dealumination and subsequent agglomeration of large PdO particles led to the significant loss of the storage capacity under harsh hydrothermally aging conditions. Therefore, it is highly desirable to devote more efforts to improving the hydrothermal stability of Pd/SSZ-13 for the practical application of PNA.

So far, some strategies have been developed to enhance the hydrothermal stability of Al-rich zeolites [22]. Among the reported approaches, the incorporation of extra-framework cations has been attested as an effective method to increase the stability of the zeolite framework [23,24]. For instance, Zhao et al. [25] reported that residual Na cations protected the framework Al of zeolite from dealumination under steaming conditions. Thus, a small amount of residual Na can increase both the hydrothermal stability and activity of Cu-based SSZ-13 (Cu/SSZ-13) for NH_3-SCR reaction. Chen et al. [26] further emphasized the necessity and feasibility of Na co-cations on Cu/SSZ-13. They reported that the existent of residual Na cations preserved the Si-O(H)-Al bonds of SSZ-13 after hydrothermal aging treatment. Although effects of co-cations on the framework structure and catalytic activity of Cu/SSZ-13 in NH_3-SCR reactions have been investigated, how the Na as co-cations affecting metal-based zeolites for application in PNA has been seldom reported. Thus, it is necessary to investigate the impact of co-cations on Pd/zeolites for low-temperature NO adsorption, thereafter guiding to promote the hydrothermal stability and activity of PNA materials.

In the present work, Pd/Na-13 was synthesized and then hydrothermally aged at 750, 800, and 850 °C for 12 h. The low-temperature NO adsorption performance was investigated. For comparison, Pd/NH_4-13 with similar Pd contents was prepared and investigated under the same condition. To reveal the effect of Na co-cations, multiple characterizations were implemented to investigate the textural properties of zeolite and physicochemical properties of active sites, such as Brunauer-Emmett-Teller (BET), X-ray diffraction (XRD), ^{27}Al magic angle spinning nuclear magnetic resonance (^{27}Al MAS NMR), scanning transmission electron microscopy (STEM), hydrogen temperature-programmed reduction (H_2-TPR), and in situ diffuse reflectance infrared Fourier transform spectroscopy (DRIFTS). The focus of this study is to reveal the importance of Na co-cations and to provide guidance for improving the hydrothermal stability and activity of Pd/SSZ-13 for application during the vehicle cold-start period.

2. Experimental

2.1. Catalyst preparation

Na-SSZ-13 (Si/Al= 10) was synthesized using the method reported by our group [3]. The materials and synthetic details are given in supplementary materials. NH_4-SSZ-13 was prepared by an ion-exchange process of the Na/SSZ-13 with NH_4Cl aqueous at 80 °C for 3 h and repeated twice to get rid of Na ions. Afterward, 1.0 wt% Pd was loaded into Na-SSZ-13 and NH_4-SSZ-13 via incipient wetness impregnation (IWI) with Pd$(NO_3)_2$ solution, and stirred with a glass rod for 8 h at room temperature intermittently. At the end of each stir, the mixture was sealed with plastic wrap and placed at room temperature. After Pd

loading, the samples were dried at 100 °C for 12 h in the oven and then calcined at 500 °C in the air for 5 h. The prepared samples were denoted as Pd/Na-13 and Pd/NH_4-13, respectively. To avoid confusion, the prepared Pd/Na-13 and Pd/NH_4-13 were denoted as Pd/Na-13-F and Pd/NH_4-13-F (F: fresh), respectively.

The hydrothermal aging (HTA) treatment was performed in a quartz tube containing 10% H_2O at 750, 800, or 850 °C for 12 h, respectively. The aged Pd/Na-13 samples that are treated at different HTA temperatures were denoted as Pd/Na-13–750A, Pd/Na-13–800A, and Pd/Na-13–850A (A: aged), respectively. Likewise, the aged Pd/NH_4-13 samples were named Pd/NH_4-13–750A, Pd/NH_4-13–800A, and Pd/NH_4-13–850A, respectively.

2.2. Catalyst characterization

The chemical compositions were conducted by inductively coupled plasma optical emission spectrometry (ICP-OES, ICAP 7000). X-ray fluorescence (XRF, EAGLE III) was carried out to measure the Si/Al ratios. The crystal phases of prepared samples were probed by X-ray diffraction (XRD, SmartLab-SE) using Cu Kα radiation ranging from 5° to 50°. Pore volume and BET surface area were detected by nitrogen adsorption at − 196 °C using Micromeritics ASAP 2420, 56 N_2 physisorption points were collected. The solid-state ^{27}Al magic angle spinning nuclear magnetic resonance (MAS NMR) using catalyst powder was conducted on a Bruker Advance 600 MHz spectrometer (Bruker Company, Karlsruhe, Germany) with BBO MAS probe operating at a magnetic field strength of 14.1 T. The ^{27}Al MAS NMR spectra were obtained by small-flip angle technique with a pulse length of 0.4 μs ($<\pi/12$) and a recycle delay of 0.5 s. The magic angle spinning rate for ^{27}Al MAS NMR was set to 12 kHz, and ^{27}Al chemical shifts was referenced to 1 M Al $(NO_3)_3$ aqueous solution (0 ppm). All spectra are normalized according to the weight of sample used for analysis and the fitted function is Gaussian function. Scanning transmission electron microscopy (STEM) and energy-dispersive X-ray spectroscopy (EDX) elemental maps were carried out on Tecnai G2 F30 (FEI, Holland) microscope with high angle annular dark-field (HAADF) detector microscope with inner collection angle of 52 mrad, the analysis was operated at accelerating voltage of 300 kV. X-ray photoelectron spectroscopy (XPS) was conducted on Thermo ESCALAB 250XI. The C 1 s peak at 284.8 eV was used as a criterion to correct the binding energy of the prepared samples. And the deconvolution of peaks was performed by XPSPEAK41 software with Gaussian-Lorentzian function. The temperature-programmed desorption of ammonia (NH_3-TPD) was performed on a Micromeritics AutoChem 2920 analyzer. Firstly, ~50 mg sample was heated up to 500 °C for pretreatment to remove the adsorbed species. Secondly, the adsorption of NH_3 was performed in a flowing 10% NH_3/Ar (30 mL min^{-1}) at 100 °C for one hour. Finally, after purging the sample in flowing Ar with flow rate of 25 mL min^{-1} for one hour, the desorption of NH_3 was performed from 100° to 600°C with a ramping rate of 10 °C min^{-1}. The profiles were recorded with a thermal conductivity detector (TCD). Hydrogen temperature-programmed reduction (H_2-TPR) was also performed on Micromeritics AutoChem 2920 chemisorption analyzer. ~50 mg sample was pretreated in the above same way. After cooling down, H_2-TPR was conducted in a flowing 10% H_2/Ar (10 mL min^{-1}) with a ramp of 10 °C min^{-1} from 50° to 250°C.

2.3. Diffuse reflectance infrared Fourier transform spectroscopy (DRIFTS)

In situ DRIFTS experiments were conducted on a Nicolet iS50 with an MCT/A detector. The sample was heated up to 400 °C for pretreatment in the flow of 10% O_2 with N_2 balance, the total flow rate is 50 mL min^{-1}. After cooling down to a specified temperature, the background spectra were collected. For NO-DRIFTS experiments, the spectra of background and NO_x adsorption were collected with the introduction of 1000 ppm NO at 100 °C. As for CO-DRIFTS experiments, the spectra

were obtained at 30 °C with the presence of 1000 ppm CO after pretreatment.

2.4. NO$_x$ adsorption and desorption study

A plug flow reactor system was used to test the NO$_x$ storage and release properties. The sample (120 mg, 60–80 mesh) was first pretreated at 500 °C under flowing gas of 10% O$_2$ in N$_2$ for 30 min, the total flow rate is 200 mL min^{-1}. A K-type thermocouple located near the sample was used to monitor the temperature. Before adsorption, the feed gas runs through the bypass line. The gas feed containing 200 ppm NO and 5% H$_2$O was introduced. After stabilization, the adsorption process was initiated by switching the gas mixture to the reaction tube and kept for 10 min. Afterward, the reactor was heated up to 550 °C with a ramping rate of 10 °C min^{-1}. The experimental procedure of NO$_x$ adsorption and desorption can be found in Fig. S1. The outlet NO$_x$ concentration was recorded by an online MKS MultiGas 2030 FTIR gas analyzer.

The amount of NO$_x$ storage and release was calculated from an integration of the adsorption-desorption profile. As shown in Fig. S2, the negative region below 200 ppm was divided into two peaks to distinguish the amount of adsorption at different stages, including peak A (~100 °C) and B (>100 °C). The amount of NO$_x$ desorption was estimated by integrating the positive peak above 200 ppm (peak C) formed in the desorption stage. More detailed analysis of peak area is depicted in Fig. S2. The amount of NO$_x$ adsorbed (NO$_x$ ads) was calculated according to the following equation.

$$Q_{NO_x} = \frac{10^{-6} F \int_0^t |F_{in} - F_{out}| dt}{22.4 \ m} \times 10^3$$

Where Q_{NO_x} (μmol g^{-1}) refers to the amount of NO$_x$ adsorption or desorption. F (mL min^{-1}) represents the gas flow. F_{in} (ppm) is the initial NO$_x$, while F_{out} (ppm) is the outlet NO$_x$. The m (g) is the weight of sample, and t (min) represents the duration of adsorption or desorption process.

In these experiments, NO$_x$ storage efficiency (NSE) refers to the percentage of stored NO$_x$ which passes over the sample. And the NSE is calculated according to the following equation.

$$NSE = (1 - \frac{\int_0^t F_{out} dt}{\int_0^t F_{in} dt}) \times 100\%$$

where t (min) represents the time of NO$_x$ adsorption, F_{out} (ppm) is the outlet NO$_x$, while F_{in} (ppm) is the inlet NO$_x$ during NO$_x$ storage.

3. Results

3.1. Characterizations of prepared samples

3.1.1. ICP-OES and N$_2$-physisorption results

The chemical compositions of Pd/Na-13 and Pd/NH$_4$-13 were analyzed by ICP-OES. As listed in Table 1, all the samples show a similar Pd content of ~ 0.8 wt%. The contents of Na in Pd/Na-13 and Pd/NH$_4$-13 are approximately 2.8 wt% and 0.1 wt%, respectively. As reported by Zhao et al. [25], the Na$^+$ contents in Cu/SSZ-13 are less than 0.1 wt% and their effects could be ignored. It is noted that the effect of Na is negligible in Pd/NH$_4$-13, in consideration of its minimal Na content (0.1 wt%).

The N$_2$-physisorption measurement was carried out to investigate the textural properties of the prepared samples [27]. The results in Table 1 show that Pd/Na-13-F possesses a surface area of 520 m^2 g^{-1} and a micropore volume of 0.27 cm^3 g^{-1}. After HTA treatment at 750 °C, both the surface area and micropore volume slightly decrease, while an obvious decrease appears when increasing the HTA temperature up to 800 and 850 °C. Compared to Pd/Na-13-F, Pd/Na-13–850A exhibits a surface area of 373 m^2 g^{-1} and micropore volume of 0.20 cm^3 g^{-1}, reducing by 28% and 26%, respectively. For Pd/NH$_4$-13, the HTA treatment also leads to a slight decrease in both surface area and micropore volume. However, the surface area and micropore volume of aged Pd/Na-13 are always lower than Pd/NH$_4$-13 after HTA treatment under the same conditions. The Na co-cations in Pd/Na-13 could have a negative influence on surface area and micropore volume during harsh HTA treatment, which is in agreement with the literature reported by Cui et al. [28]. The decreased surface area and micropore volume of aged Pd/NH$_4$-13 samples could result from either the damage of the framework or the block of the zeolite pore by metal clusters. The detail will be discussed further in combination with the results of the following characterization.

3.1.2. XRD results

XRD measurements were widely used to detect the structural

Table 2
Assignments of peaks associated with NO-DRIFTS and CO-DRIFTS.

Adsorbate	Band (cm^{-1})	Assignment	References
NO	2173	NO$^+$ species located in Brønsted acid sites	[20,31]
	1863	Pd^{2+}-NO	[35–37]
	1809	Pd$^+$-NO	[39,44]
CO	2171/2161	Pd^{2+}-CO	[35,37]
	2148	Pd^{2+}(OH)(CO)	[42,44]
	2105	Pd^0-CO	[37,43]

Table 1
Chemical compositions and textural properties of Pd/Na-13 and Pd/NH$_4$-13.

Sample	Pd loading[a] (wt%)	Na loading[a] (wt%)	S$_{BET}$[b] (m^2 g^{-1})	V$_{micro}$[c] (cm^3 g^{-1})	Relative crystallinity[d] (%)
Pd/Na-13-F	0.81	2.77	520	0.27	100
Pd/Na-13–750A	0.81	2.75	448	0.24	95
Pd/Na-13–800A	0.83	2.82	418	0.22	92
Pd/Na-13–850A	0.82	2.83	373	0.20	88
Pd/NH$_4$-13-F	0.82	0.11	533	0.28	100
Pd/NH$_4$-13–750A	0.83	0.12	504	0.27	74
Pd/NH$_4$-13–800A	0.80	0.10	477	0.26	70
Pd/NH$_4$-13–850A	0.81	0.13	465	0.24	67

Relative crystallinity (%) = $\frac{\text{Sum of the intensities of the peaks at } 2\theta = 9.7°, 20.9° \text{ and } 31.1° \text{ after HTA treatment}}{\text{Sum of the intensities of the peaks at } 2\theta = 9.7°, 20.9° \text{ and } 31.1° \text{ before HTA treatment}} \times 100\%$

[a] Element content obtained from ICP-OES
[b] Surface area calculated from N$_2$ adsorption/desorption isotherms at 77.2 K using BET equation
[c] t-Plot micropore volume calculated from N$_2$ isotherm at $P/P_0 = 0.993$, 77.2 K
[d] Assuming the crystallinity of Pd/Na-13-F and Pd/NH$_4$-13-F samples to be 100% and the relative crystallinity of the other samples after hydrothermal aging treatment calculated with the following equation [27]:

properties of crystals. As presented in Fig. 1, both Pd/Na-13 and Pd/NH$_4$-13 before and after HTA treatment display identical chabazite (CHA) diffraction peaks at 9.7°, 20.9° and 31.1° (JCPDS 52–0784) [19, 21]. It suggests that there are no obvious damages to the long-range order structure of aged Pd/Na-13 and Pd/NH$_4$-13 [29]. Besides, no obvious peaks belonging to PdO at 33.9° (JCPDS 43–1024) are observed in the XRD patterns of all samples [19,29], indicating that the Pd species is well-dispersed or the amount of PdO is too low to be detected by XRD measurement. It is noted that metallic Pd originated from the decomposition of PdO is clearly observed at 40.1° (JCPDS 65–6174) in the XRD pattern of Pd/Na-13–850A [19,30], indicating the sintering of Pd due to the harsh hydrothermally aging conditions. The Pd sintering of Pd/Na-13–850A will be discussed in Section 3.2. In addition, the relative crystallinity was calculated by summing the intensities of the peaks at 2θ = 9.7°, 20.9° and 31.1° [27]. As listed in Table 1, 88% of the relative crystallinity remains for the Pd/Na-13–850A, while Pd/NH$_4$-13–850A shows a relative crystallinity of 67%. According to the changes in relative crystallinity, it is obvious that more harsh damage occurs on Pd/NH$_4$-13 than on Pd/Na-13. It signifies that the Na co-cations in Pd/Na-13 could stabilize the structure of zeolite to a certain extent during HTA treatment.

3.1.3. ^{27}Al MAS NMR results

To further probe the subtle changes in the structure of Pd/Na-13 and Pd/NH$_4$-13, solid-state ^{27}Al MAS NMR measurement was carried out. As shown in Fig. 2a, the fresh and aged Pd/Na-13 samples exhibit Al coordination centered at ~60 ppm which is assigned to tetrahedrally coordinated framework Al (Al$_{tetra}$), while the peak at around 45 ppm is another Al$_{tetra}$ in differentiable environments [30]. And the peaks at −20 ppm are spinning sidebands. With the increasing of HTA temperature, there are no obvious changes observed in the ^{27}Al MAS NMR spectra of Pd/Na-13 samples, indicating that the framework Al of Na-SSZ-13 remains stable tetrahedrally coordination after severe HTA treatment. Note that the relative crystallinity of Pd/Na-13–850A decreases by 12% compared with fresh Pd/Na-13, while the extra-framework Al is not formed. It may due to the negative effect of Na poisoning on the intensity of XRD diffraction peaks. However, significant changes are observed in the ^{27}Al MAS NMR spectra of aged Pd/NH$_4$-13 samples. The spectrum of Pd/NH$_4$-13-F shows a peak centered at ~60 ppm which is similar to that of Pd/Na-13-F. Note that the Pd/NH$_4$-13-F contains peak at~ 4 ppm assigned to extra-framework Al and no such features are obvious for the Pd/Na-13-F. The formation of extra-framework Al may occur during the process of the incipient wetness impregnation with Pd(NO$_3$)$_2$ solution and subsequent calcination which is also observed by Khivantsev' s group [30]. In comparison to Pd/NH$_4$-13-F, a much stronger peak at~ 4 ppm and a new peak at ~ 35 ppm are detected in Pd/NH$_4$-13–750A, which can be assigned to octahedrally extra-framework Al (Al$_{octa}$) and penta-coordinated

framework Al (Al$_{penta}$), respectively [21,31]. As the temperature increasing to 800 and 850 °C, it can be found that the intensity of Al$_{tetra}$ decreases gradually. To quantize the changes, the correspondingly relative proportion of different Al coordination was calculated using spectral deconvolution (Table S1 and Fig. S3). The percentage of Al$_{tetra}$ significantly decrease to 47% and 43% for Pd/NH$_4$-13–800A and Pd/NH$_4$-13–850A, respectively. Therefore, the ^{27}Al MAS NMR results show that minor changes are found in aged Pd/Na-13, while the Pd/NH$_4$-13 suffers from more severe dealumination during HTA treatment. ^{27}Al MAS NMR analysis manifests that Na co-cations are beneficial to preserving the framework Al of zeolite, thereby sustaining the structure of zeolite during HTA treatment.

3.1.4. DRIFTS results

DRIFTS measurements were used to detect OH vibrational of Pd/Na-13 and Pd/NH$_4$-13 samples. As depicted in Fig. 3a, four bands of OH vibration at 3700, 3648, 3603, and 3581 cm^{-1} are detected in fresh and aged Pd/Na-13. Among them, the bands at 3700 and 3648 cm^{-1} are attributed to the vibration of Si-OH and Al-OH, respectively [21,32]. The weak peaks at 3603 and 3581 cm^{-1} are assigned to Si-O(H)-Al [26, 32]. As for the spectra of Pd/NH$_4$-13-F (Fig. 3b), the Al-OH (3660 cm^{-1}) and Si-O(H)-Al (3609 and 3583 cm^{-1}) are observed. It shows that Pd/NH$_4$-13-F possess more Si-O(H)-Al than Pd/Na-13-F, which is in good agreement with NH$_3$-TPD results (Fig. S4 and Table. S2). After HTA treatment at 750 and 800 °C, Pd/Na-13 samples exhibit a slight decline of Si-O(H)-Al band, while the bond in Pd/NH$_4$-13 decreases significantly and almost disappears after HTA treatment at 800 °C. Therefore, combined with the results of DRIFTS and NH$_3$-TPD, the Na co-cations can protect Si-O(H)-Al from severe destruction, which is consistent with ^{27}Al MAS NMR and XRD results.

3.2. Characterizations of Pd species

3.2.1. HAADF-STEM and EDX mapping results

HAADF-STEM images of Pd/Na-13 and Pd/NH$_4$-13 samples are shown in Fig. 4a. Pd/Na-13-F shows the distribution of PdO nanoparticles with a size of ~1 nm, owing to the lack of available ionic positions for the exchange of Pd ions [33]. Whereas abundant PdO nanoparticles have transformed into highly dispersed Pd cations after HTA treatment at 750 and 800 °C (Figs. 4b and 4c). The enhanced dispersion of Pd cations after HTA treatment in this work agrees well with previous reports [19,20,29]. When the temperature is up to 850 °C, large metal nanoparticles are observed in Pd/Na-13–850A with an average size of 2.3 nm (Fig. 4d and S5a). In this case, we speculate that Na ions fall away from ionic exchange sites of Na-SSZ-13 and poison Pd species in the Pd/Na-13–850A during HTA treatment at 850 °C, thereby leading to the aggregation of PdO [34]. With the promotion of H$_2$O through hydrothermal aging at 850 °C for 12 h, the PdO decomposes
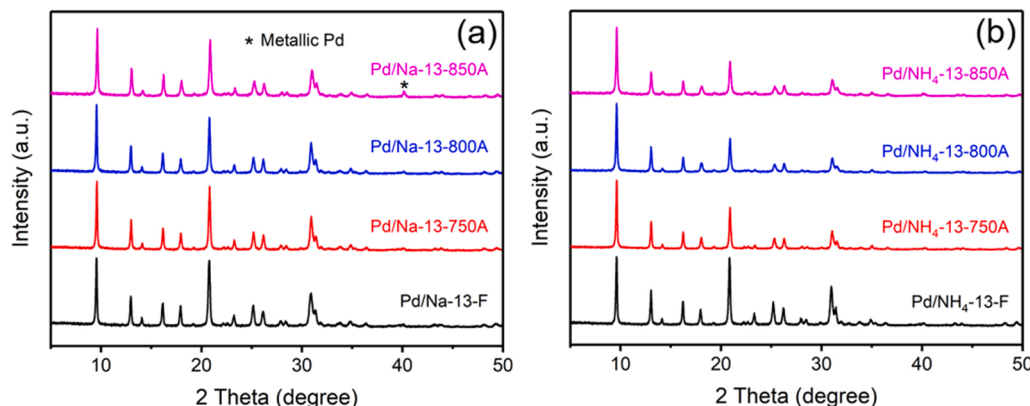

Fig. 1. XRD patterns of Pd/Na-13 (a) and Pd/NH$_4$-13 (b) samples before and after HTA treatment.
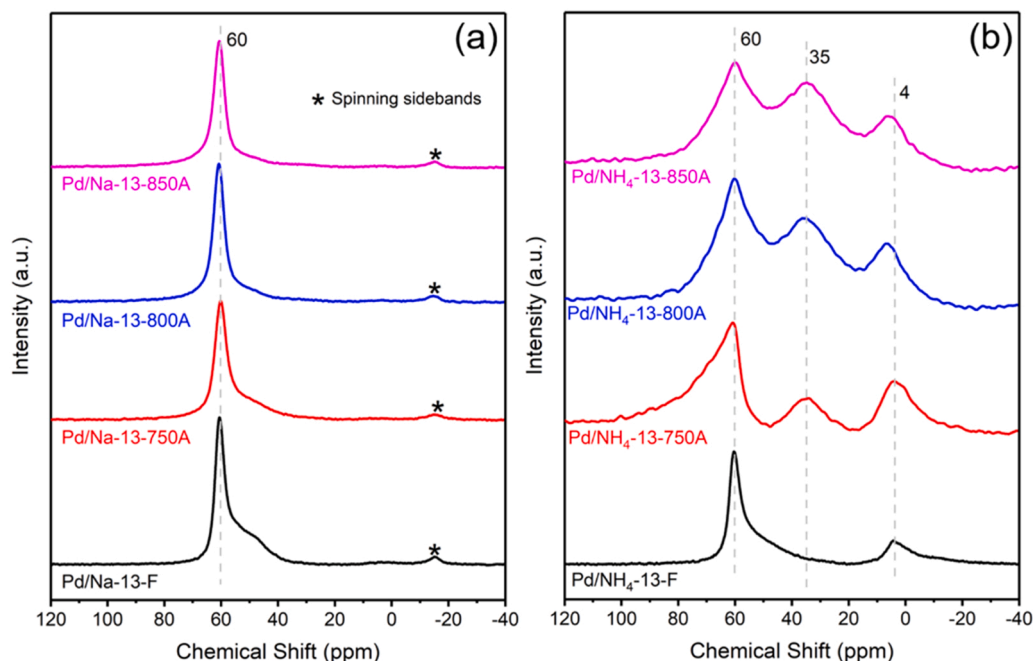
Fig. 2. ^{27}Al MAS NMR spectra of Pd/Na-13 (a) and Pd/NH$_4$-13 (b) samples before and after HTA treatment.
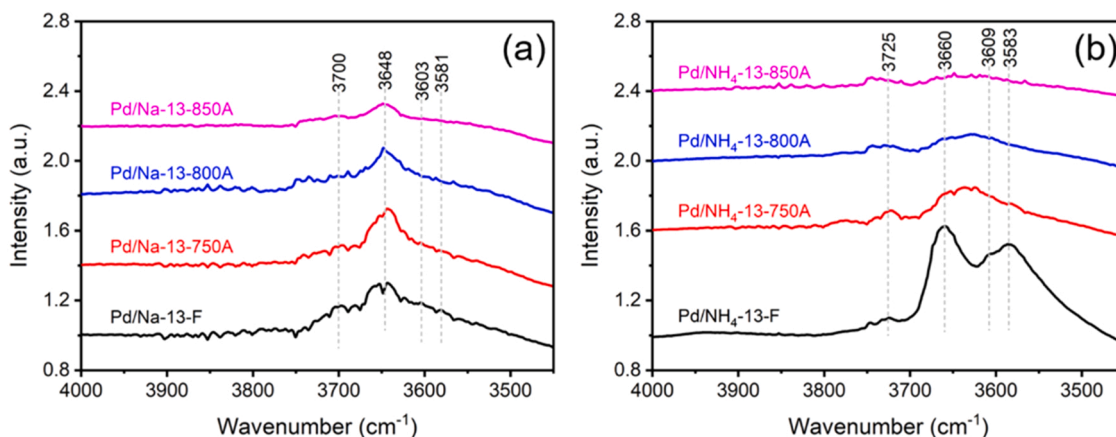

Fig. 3. DRIFTS spectra of Pd/Na-13 (a) and Pd/NH$_4$-13 (b) samples before and after HTA treatment with a flow of 1000 ppm NH$_3$ and N$_2$ measured at 100 °C. Total flow rate was 50 mL min^{-1}.

into metallic Pd and forms large metal particles, which is also evidenced by the peak at 40.1° in the XRD pattern [21,30]. As for Pd/NH$_4$-13 samples, the Pd/NH$_4$-13-F sample reveals homogeneously dispersed Pd over the NH$_4$-SSZ-13 support (Fig. 4e). Well-dispersed Pd is observed in Pd/NH$_4$-13 after HTA treatment at 750 and 800 °C (Figs. 4f and 4g). When the HTA temperature increases to 850 °C, the aggregated metal nanoparticles with a particle size of 1.0 nm (Fig. S5b) are shown due to the loss of framework Al sites (Fig. 4h).

The EDX mapping was performed to visualize the distribution of elements in the Pd/Na-13–750A. In Fig. 5, uniform distribution of Si, Al, O, and Na is observed throughout SSZ-13 crystals. Particularly, highly dispersed Pd is also observed in Fig. 5c. The distribution of elements of Pd/Na-13–850A was also determined by EDX. As shown in Fig. S6, Pd/Na-13–850A shows heterogeneously distributed Na. Therefore, it is possible that there is poisoning effect of Na in Pd/Na-13–850A.

Taking into account the results of ^{27}Al MAS NMR and XRD, Na cations can stabilize the framework of SSZ-13 during HTA treatment. The lower surface area and micropore volume of Pd/Na-13 than Pd/NH$_4$-13 samples after HTA treatment are attributed to the influence of Pd

sintering. Due to the Na poisoning by HTA treatment, the large metal particles derived from the decomposition of PdO in Pd/Na-13–850A distribute on the external surface and block the channels of SSZ-13 zeolite, thus leading to decreased surface area and micropore volume after HTA treatment.

3.2.2. XPS results

The XPS spectra of Pd 3d were recorded to identify the Pd oxidation state of Pd/Na-13 and Pd/NH$_4$-13. As shown in Fig. S7a, the spectra of Pd/Na-13 samples can be deconvoluted into four peaks, and the main peaks are located at around 336.0 (3d$_{5/2}$) and 341.7 eV (3d$_{3/2}$), which can be assigned to Pd^{2+} species [19,35]. The peaks at approximately 338.8 (3d$_{5/2}$) and 345.5 eV (3d$_{3/2}$) are assigned to Pd^{4+} species [36]. Besides, the spectrum of Pd/Na-13–850A shows the two peaks assigned to metallic Pd at 341.0 and 335.3 eV [10], respectively, which is in line with the result of XRD pattern (Fig. 1a). It is obvious that Pd^{2+} species are dominant in both fresh and aged Pd/NH$_4$-13 samples (Fig. S7b).
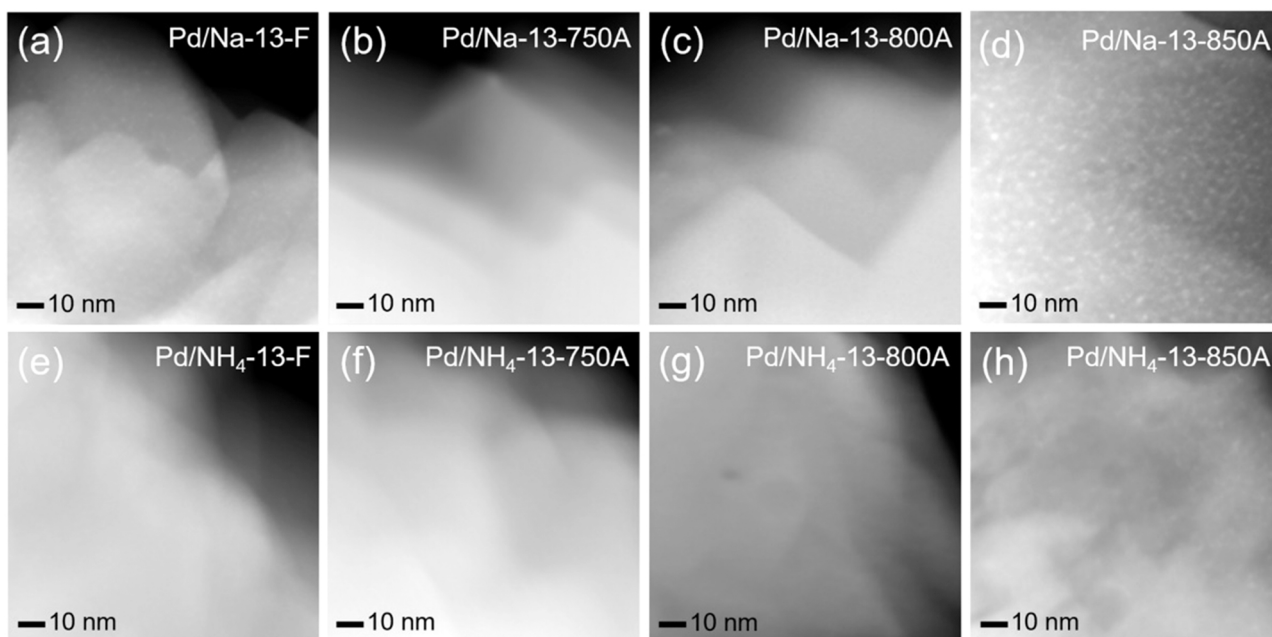
Fig. 4. HAADF-STEM images of Pd/Na-13 (a-d) and Pd/NH$_4$-13 (e-h) samples before and after HTA treatment.
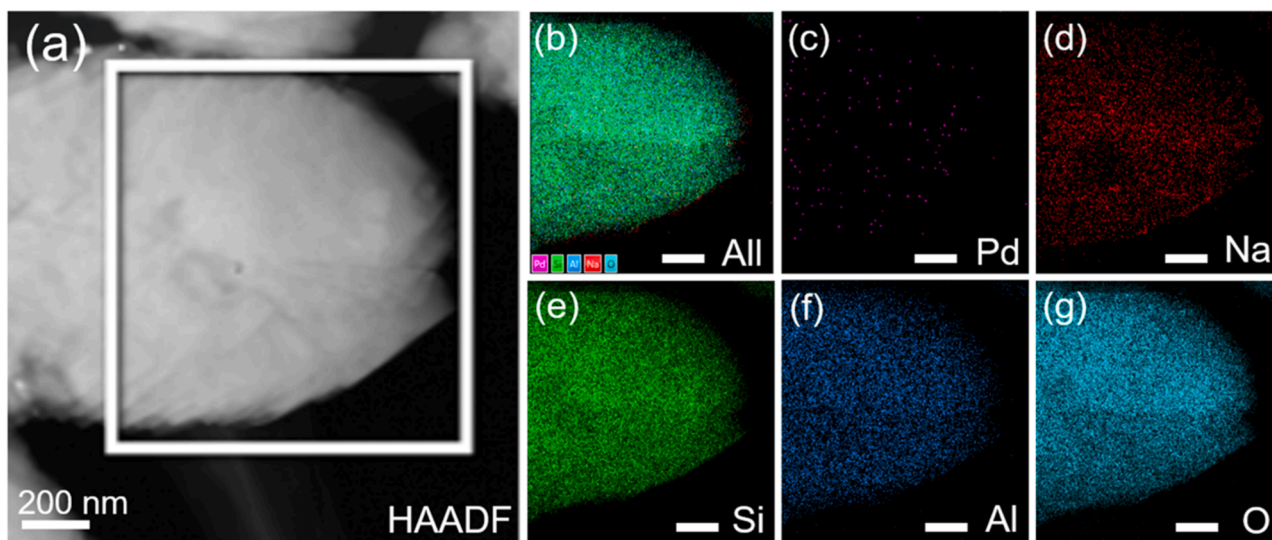

Fig. 5. HAADF-STEM image (a) and EDX mapping (b-g) of Pd/Na-13–750A (the size bars represent 200 nm).

3.2.3. H$_2$-TPR results

Note that TEM imaging has been often used to detect Pd dispersion of Pd/SSZ-13 [20,21]. However, high-energy electrons of TEM imaging could destroy the micropores of SSZ-13 which induced Pd sintering severely [8,37]. Therefore, the Pd dispersion of Pd/SSZ-13 was analyzed combined with H$_2$-TPR analysis. H$_2$-TPR analysis was performed to investigate the reducibility of different Pd species in Pd/SSZ-13 samples, and the profiles are displayed in Fig. 6. The H$_2$-TPR profile of Pd/Na-13-F shows two reduction peaks, including a negative peak at around 89 °C and a positive peak at about 106 °C (Fig. 6a), which is similar to the results reported by Ji et al. [35]. The former is attributed to the decomposition of PdH$_x$ [37,38]. The latter is assigned to the reduction of Pd ions to metallic Pd [39,40]. For Pd/Na-13–750A and Pd/Na-13–800A, the reduction peaks originated from Pd ions become strong and shift to the high temperature of 121 °C, indicating the existence of more stable Pd ions after HTA treatment at 750 and 800 °C. However, the desorption of H$_2$ derived from PdH$_x$ remarkably increases

and the consumption of H$_2$ originated from Pd ions significantly decreases in Pd/Na-13–850A. Due to the limitation of equipment, we cannot provide the H$_2$-TPR profiles at lower temperatures. As reported, Lee et al. [41] and Shan et al. [20] observed the reduction of the bulk PdO to metallic Pd at below 50 °C. Therefore, we propose that the reduction of PdO to metallic Pd in H$_2$-TPR has already occurred at a temperature below 50 °C. Note that metallic Pd was detected by XRD and XPS measurements in Pd/Na-13–850A, it can be deduced that all the metallic Pd for forming PdH$_x$ are derived from the decomposition of PdO during HTA treatment at 850 °C. Therefore, the negative peak originated from the decomposition of PdH$_x$ can be indirectly correlated to aggregated metallic Pd particles that have been observed in HAADF-STEM images (Fig. 4). Thus, the larger negative peak in the H$_2$-TPR profiles manifests the presence of more metallic Pd particles. As shown in Fig. 5b, Pd/NH$_4$-13-F exhibits a strong reduction peak of Pd cations. As expected, more Pd ions are observed after activation by hydrothermal treatment at 750 and 800 °C. While the increasing release
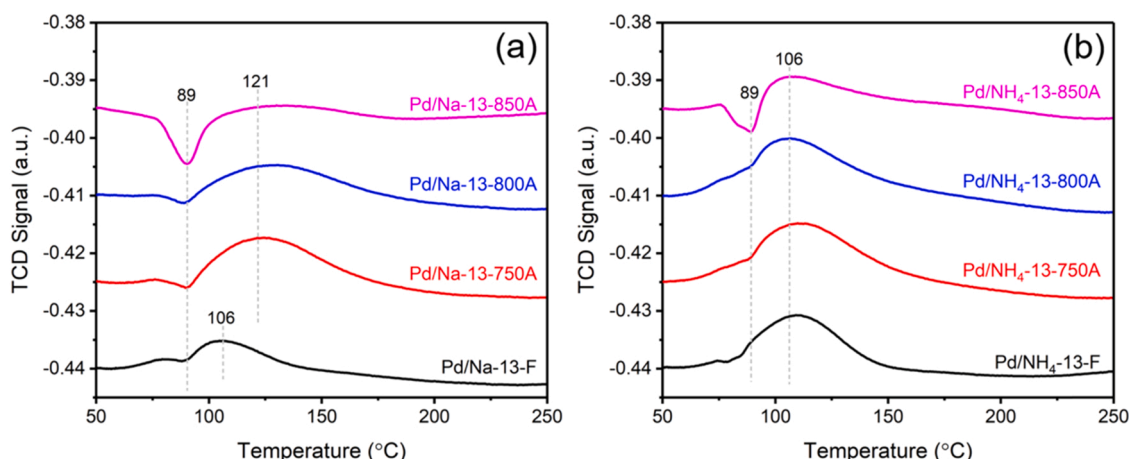
Fig. 6. H$_2$-TPR profiles of Pd/Na-13 (a) and Pd/NH$_4$-13 (b) samples before and after HTA treatment.

of H$_2$ in Pd/NH$_4$-13–850A indicates the aggregation of metal nanoparticles, which is in line with the result of HAADF-STEM analysis (Fig. 4h). Additionally, the profile of Pd/NH$_4$-13–850A shows a small peak at 75 °C which is assigned to the reduction of PdO, indicating the presence of smaller PdO particles after HTA treatment at 850 °C [20].

3.2.4. NO-DRIFTS results

NO-DRIFTS experiments were carried out to recognize Pd species in Pd/Na-13 and Pd/NH$_4$-13. As depicted in Fig. 7, three absorption peaks are observed at 2173, 1863, and 1809 cm^{-1}. The peak at 2173 cm^{-1} is ascribed to the NO$^+$ adsorbed on Brønsted acid site (BAS) [31,42]. The peaks at 1863 and 1809 cm^{-1} are attributed to Pd^{2+}-NO and Pd$^+$-NO complex, respectively [20,36,39]. Specifically, the two peaks indicate the abundance of Z$^-$Pd^{2+}Z$^-$ and Z$^-$[Pd(II)OH]$^+$ (Z$^-$ represents the [Si-O-Al]$^-$), which are stabilized by two proximate Al sites and one isolated Al site in Pd/SSZ-13, respectively [20,21]. Previous studies proposed that the formation of Pd^{2+}-NO and Pd$^+$-NO is attributed to the NO adsorption on Z$^-$Pd^{2+}Z$^-$ and Z$^-$[Pd(II)OH]$^+$ [31,42]. Note that the assignment of peak at 1809 cm^{-1} may be in debate in previous study. However, Khivantsev et al. [13] has detected the presence of Pd$^+$ evidenced from in situ EPR studies of Pd/SSZ-13 in their latest research. Meanwhile, they have also proved that Pd$^+$-NO is resulting from the reduction of Z$^-$[Pd(II)OH]$^+$ due to no Pd$^+$ is detected at the beginning of experiment.

The NO-DRIFT spectra in Fig. 7 show that the Pd ions distributed differently in the aged Pd/Na-13 and Pd/NH$_4$-13. As depicted in Fig. 7a, the bands at 1863 cm^{-1} are dominant in the aged Pd/Na-13 samples,

indicating the existence of more Pd^{2+} balanced by two proximate Al sites after HTA treatment [31]. In contrast, the spectra of aged Pd/NH$_4$-13 samples (Fig. 7b) exhibit stronger intensity at 1809 cm^{-1}, implying the presence of more [Pd(II)OH]$^+$ balanced by isolated Al sites [42–44]. Compared with the spectra of Pd/Na-13, the peaks at 2173 cm^{-1} in Pd/NH$_4$-13 samples decline rapidly or even disappear after HTA treatment, signifying that the BAS of Pd/NH$_4$-13 reduces significantly after HTA treatment, which is consistent with the aforementioned results of DRIFTS in Section 3.1.4. The different distribution of Pd-nitrosyl species probably results from different concentrations of paired Al sites in the SSZ-13 zeolite after hydrothermal aging treatment.

3.2.5. CO-DRIFTS results

DRIFTS measurements of CO adsorption were conducted to further characterize Pd species of Pd/Na-13 and Pd/NH$_4$-13, and the spectra are given in Fig. 8. The bands at 2171 and 2161 cm^{-1} can be ascribed to Pd^{2+}-CO, i.e., CO adsorbs on Z$^-$Pd^{2+}Z$^-$ site that is stabilized by paired Al sites [36,43,44]. Another adsorption peak at 2148 cm^{-1} is attributed to Pd^{2+}(OH)(CO) which is CO adsorption on [Pd(II)OH]$^+$ [21,36]. The peak at 2105 cm^{-1} is ascribed to Pd^0-CO, originating from the reduction of PdO to Pd^0 by CO [36,43]. For the spectra of the Pd/Na-13-F, the peak with strong intensity at 2148 cm^{-1} is observed, indicating abundant Pd ions are stabilized by one Al site in Pd/Na-13-F. After HTA treatment at 750 and 800 °C, all the peaks of Pd/Na-13 samples are evidently enhanced in intensity, especially the peaks with respect to Pd^{2+}-CO. The transition of Pd species monitored by CO-DRIFTS agrees with the results of NO-DRIFTS. Notably, the abundant Pd ions appear in Pd/Na-13 after
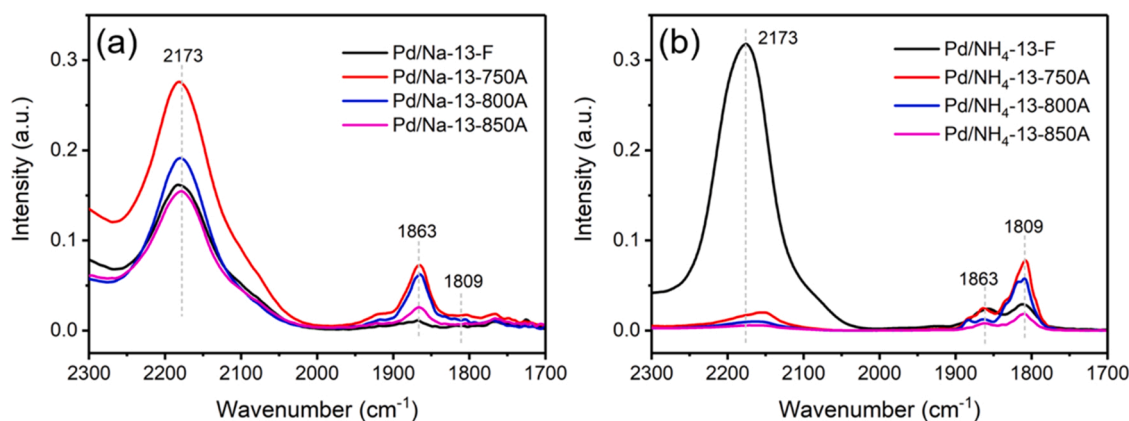

Fig. 7. In situ DRIFTS spectra of Pd/Na-13 (a) and Pd/NH$_4$-13 (b) samples with a flow of 1000 ppm NO and N$_2$ measured at 100 °C. Total flow rate was 50 mL min^{-1}.

Fig. 8. In situ DRIFTS spectra of Pd/Na-13 (a) and Pd/NH$_4$-13 (b) samples with a flow of 1000 ppm CO and N$_2$ measured at 30 °C. Total flow rate was 50 mL min^{-1}.
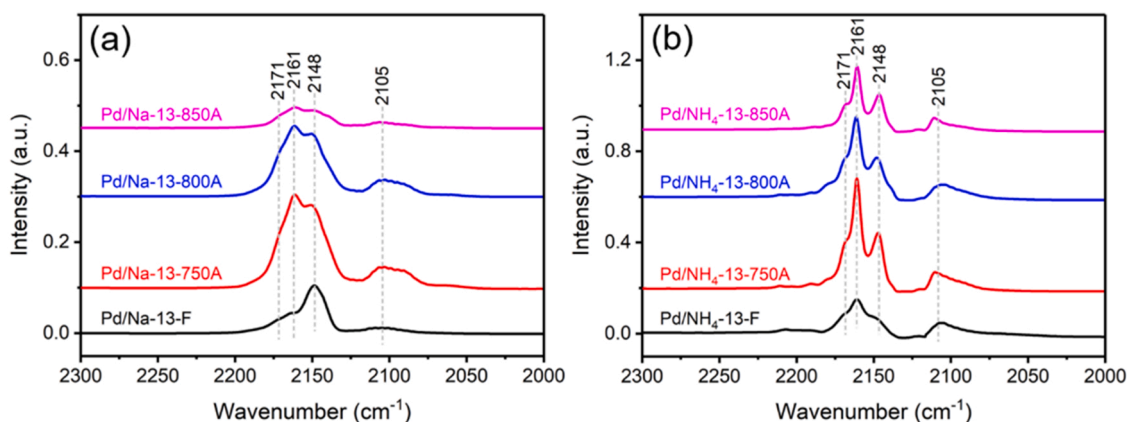
HTA treatment at 750 °C. However, a rapid decrease in the peak of Pd ions is observed in Pd/Na-13–850A, when increasing the HTA temperature to 850 °C.

In Fig. 8b, Pd/NH$_4$-13-F exhibits a relatively stronger peak of Pd^{2+}-CO than Pd/Na-13-F, due to more ion-exchange sites for Pd ions in NH$_4$-SSZ-13 [21,31]. After HTA treatment, the peak intensity of Pd^{2+}-CO evidently increases, as observed in the spectra of Pd/Na-13 HTA samples. Especially, the peaks at 2148 cm^{-1} become distinct and sharp, implying that an increasing amount of [Pd(II)OH]$^+$ are formed in the samples after HTA treatment [36,44].

3.3. Performance of NO$_x$ adsorption and release

Fig. 9 displays the NO$_x$ storage and release curves over Pd/Na-13 and Pd/NH$_4$-13. Experimental procedure of NO$_x$ adsorption and desorption is illustrated in Fig. S1. It is noted that the negative peak of NO$_x$ below 200 ppm indicates the storage of NO$_x$, and the positive peak above 200 ppm reflects the release of NO$_x$ (Fig. 9). The amount of NO$_x$ storage was estimated by integrating the negative peak below 200 ppm. The amount of NO$_x$ release was obtained by integrating the positive peak above 200 ppm in the desorption stage. More detailed analysis of peaks can be found in Fig. S2 and Table S3. To make clear the process of NO$_x$ storage and release, the curves of NO and NO$_2$ of Pd/Na-13 and Pd/NH$_4$-
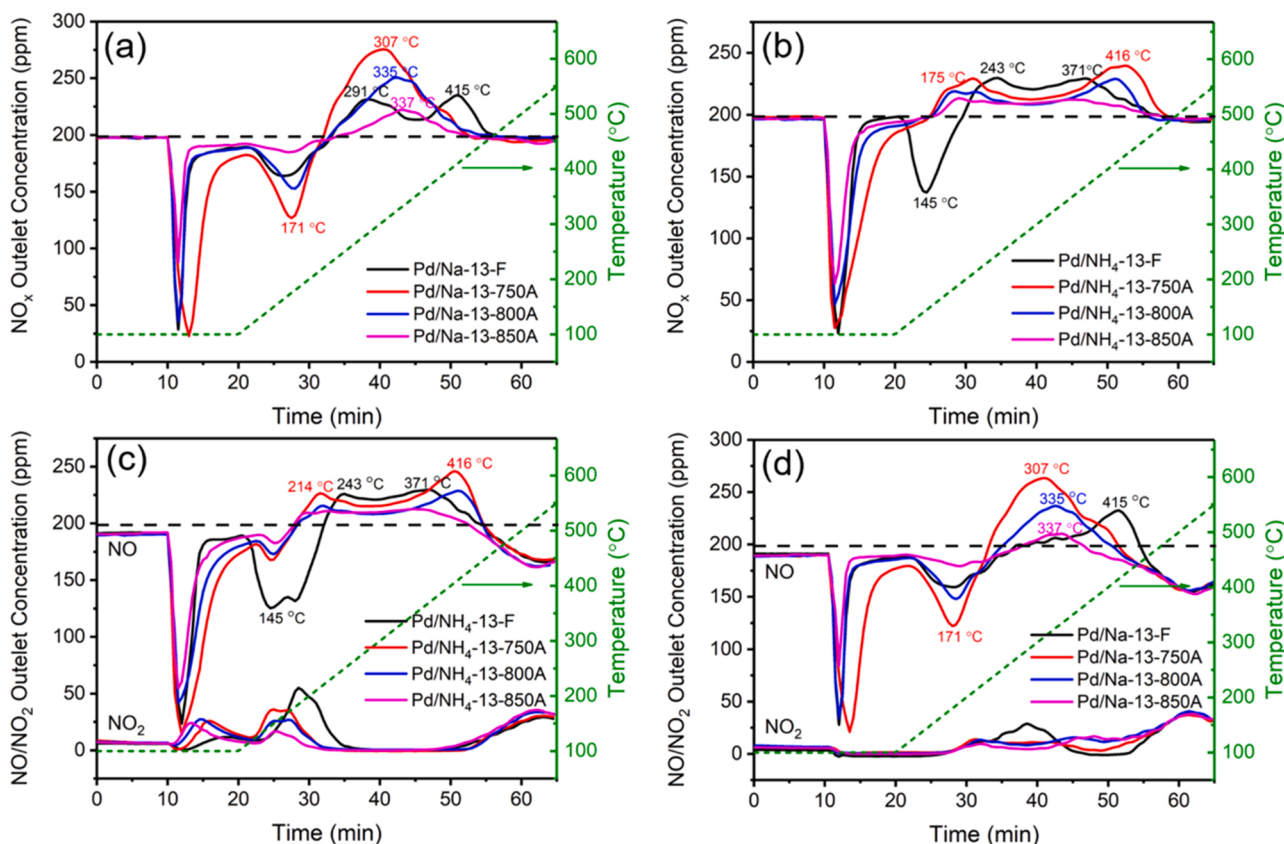

Fig. 9. The NO$_x$ profiles of Pd/Na-13 (a) and Pd/NH$_4$-13 (b) samples before and after HTA treatment for NO adsorption at 100 °C for 10 min followed with release (10 °C min^{-1} up to 550 °C). The concentrations of NO and NO$_2$ of Pd/Na-13 (c) and Pd/NH$_4$-13 (d) before and after HTA treatment during adsorption and release. Reaction conditions: 200 mL min^{-1} (200 ppm NO, 10%vol O$_2$, 5%vol H$_2$O and balanced with N$_2$). Note that during the first 10 min of data recording, the feed gas runs through the bypass line.

13 are also presented in Figs. 9c and 9d, respectively.

During the process of storage, a rapid decline of the NO_x concentration can be seen for all samples when the gas feed is switched to the reactor (Fig. 9a). The NO_x breaks through and down to a minimum in the end. After the gradual recovery of NO concentration, the second NO_x uptakes occur at around 171 and 145 °C for Pd/Na-13-F and Pd/NH$_4$-13-F, respectively. As shown in Fig. S8, the water shows a rapid decline when the gas feed is switched to the reactor at 100 °C and releases when the temperature increases, it suggests that the desorption of water from Pd sites enables the second NO_x uptakes [21,42]. Eventually, the NO_x concentration exceeds the baseline of 200 ppm and NO_x release occurs with the increasing of temperature. Both the Pd/Na-13-F and Pd/NH$_4$-13-F show two NO_x desorption peaks, indicating the presence of two kinds of Pd sites. Notably, NO_x desorption temperature is the key factor to assess the performance of PNA materials. The expected desorption temperature should fall between 250 and 350 °C to offer available storage sites for the next run. As depicted in Fig. 9a, the NO_x release curve of Pd/Na-13-F shows two peaks with maximum value at ~ 291 and 415 °C, respectively. Similar to the Pd/Na-13-F, Pd/NH$_4$-13-F exhibits two NO_x desorption peaks at ~ 243 and 371 °C in Fig. 9b. It manifests that two different Pd sites exist in both Pd/Na-13-F and Pd/NH$_4$-13-F. During the entire storage stage, the total amounts of NO_x adsorption are 42.6 and 48.3 μmol g^{-1} for Pd/Na-13-F and Pd/NH$_4$-13-F, respectively (Fig. 10). The comparison of different reported PNA materials in the literatures was listed in Table S4. It shows that the framework types of zeolites, Si/Al ratios, Pd loadings, and testing conditions can affect the NO_x uptake of PNA materials. Note that the testing conditions (i.e., H$_2$O and CO) have significant effects on the NO_x storage capacity of Pd/zeolites, which has been investigated by many groups [10,33,42]. For example, the presence of water always decreases the NO_x storage capacity of Pd/zeolites, while the CO can promote the NO_x uptake. The gas mixture in our study contains ~5% H$_2$O but without CO. It should be pointed out that the NO_x/Pd ratios of Pd/Na-13–750A and Pd/NH$_4$-13–750A are as high as 1.12 and 0.81, respectively, which are comparable to the reported PNA materials. A full comparative analysis which also includes Na-containing systems can be found in the supplementary materials.

After HTA treatment at 750 °C, both Pd/Na-13 and Pd/NH$_4$-13 show the most increase in NO adsorption capacity (Fig. 9). Pd/NH$_4$-13–750A shows significant generation of NO$_2$ which is not observed in Pd/Na-13–750A (Figs. 9c and 9d). Note that the Pd/Na-13–750A shows higher NO_x adsorption capacity than Pd/NH$_4$-13–750A. The NO_x adsorption at above 100 °C contributes to the adsorption capacity of Pd/Na-13–750A, which is important for further discussion. As seen in Fig. 10, the amounts of adsorbed NO (NO_x ads) are 85.6 and 62.8 μmol g^{-1} for Pd/Na-13–750A and Pd/NH$_4$-13–750A, respectively. As the temperature increases to 800 and 850 °C, both the Pd/Na-13 and Pd/NH$_4$-13 exhibit

Fig. 10. Amount of NO_x adsorption and NO_x/Pd of Pd/Na-13 and Pd/NH$_4$-13 samples before and after HTA treatment.

declining NO adsorption capacity. Even so, the NO_x adsorption at above 100 °C always exists in aged Pd/Na-13 (Fig. 9a).

In terms of NO_x adsorption over 100 °C for aged Pd/Na-13 and Pd/NH$_4$-13, the NO_x uptake peaks over 100 °C disappear for Pd/NH$_4$-13, while these peaks are still observed for Pd/Na-13 after HTA treatment, as shown in Fig. 9. As for the temperature of NO_x desorption, Pd/Na-13–750A shows the majority desorption of trapped NO_x at around 307 °C. While the NO_x desorption over aged Pd/NH$_4$-13 occurs out of the optimal temperature range. For instance, the Pd/NH$_4$-13–750A exhibits two NO_x desorption peaks at ~175 and 416 °C. The two interesting features will be discussed based on the difference of Pd sites in aged Pd/Na-13 and Pd/NH$_4$-13 samples.

It is of importance to assess the performance of PNA by comparing the NO_x/Pd ratio. Fig. 10 and Table S5 exhibits the calculated NO_x/Pd ratios for Pd/Na-13 and Pd/NH$_4$-13 samples. The NO_x/Pd ratios of Pd/Na-13-F and Pd/NH$_4$-13-F are 0.54 and 0.61, respectively. After HTA treatment at 750 °C, the NO_x adsorption capacities of the Pd/Na-13 and Pd/NH$_4$-13 significantly increase. The NO_x/Pd ratios of them reach the maximum of 1.07 and 0.78, respectively. As for the samples treated at temperatures above 750 °C (i.e., 800 and 850 °C), a rapid decrease of NO_x/Pd ratios occurs, resulting from the decreasing NO_x adsorption capacity. Specifically, 0.56 and 0.26 of the NO_x/Pd ratios are obtained in Pd/Na-13–800A and Pd/Na-13–850A, respectively. While the Pd/NH$_4$-13–800A and Pd/ NH$_4$-13–850A samples display the NO_x/Pd ratios of 0.49 and 0.33, respectively. Additionally, Fig. S9 displays NSE as a function of time. It shows that all samples display a significant increase in NSE and reach the maximum value during early stage of storage, and then the NSE decreases significantly with time. Note that the second increase in NSE being attributed to the additional adsorption is observed in aged Pd/Na-13 samples, while the aged Pd/NH$_4$-13 samples exhibit no increase in NSE.

4. Discussion

4.1. Enhanced stability promoted by Na co-cations

Here, we mainly discuss the promotion of hydrothermal stability of Pd/SSZ-13 promoted by Na co-cations. Based on XRD results (Fig. 1), both Pd/Na-13 and Pd/NH$_4$-13 samples display typical CHA structure, indicating that long-range order structure is well-maintained after harsh hydrothermal aging treatment. By contrast, an obvious decrease of diffraction peaks at 20.9° and 31.1° is observed in aged Pd/NH$_4$-13 samples, and the relative crystallinity of Pd/NH$_4$-13–850A decreases by 33%. Additionally, ^{27}Al MAS NMR spectra in Fig. 2b shows that Pd/NH$_4$-13 samples suffer from more severe dealumination during hydrothermal aging, and the proportion of Al$_{tetra}$ decreases with the increasing of temperature (Fig. S3 and Table S1). As reported by Zhao et al. [21], dealumination was the primary reason for the transformation of Pd^{2+} ions to PdO in Pd/SSZ-13 under harsh HTA conditions [21]. In contrast to hydrothermally aged Pd/NH$_4$-13 samples, aged Pd/Na-13 samples always possess tetrahedrally coordinated framework Al signal rather than Al$_{penta}$ and Al$_{octa}$ (Fig. 2a), indicating stable framework Al present in Pd/Na-13 after HTA treatment. Note that the remaining of Na ions is responsible for the tetrahedral co-ordination of SSZ-13. That is to say, high hydrothermal stability of SSZ-13 can be achieved with the addition of Na. Consequentially, Na co-cations can protect the structure of Pd/Na-13 from serious destruction by hydrothermal aging.

Based on DRIFTS (Fig. 3) and NH$_3$-TPD results (Fig. S4), the BAS densities of aged Pd/NH$_4$-13 samples decrease significantly even at the mild temperature of 750 °C. It indicates that the Pd/NH$_4$-13 samples suffer more severe destruction on the zeolite framework after HTA treatment, which is in line with the reported studies [20,31]. Whereas, the aged Pd/Na-13–750A shows negligible loss of BAS, implying that Na co-cations play an indispensable role in protecting the BAS during hydrothermal aging treatment. Thus, more ion-exchange sites in aged Pd/Na-13 samples can be retained for Pd cations. As a result, the
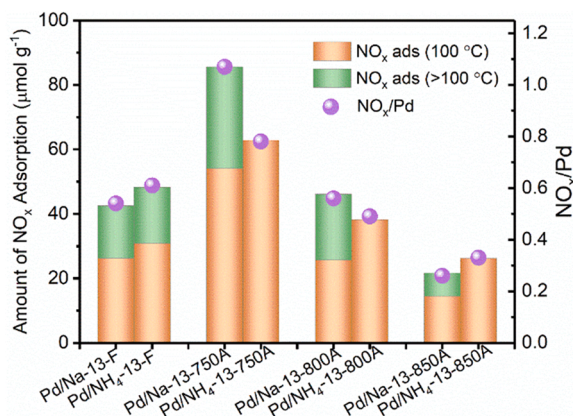
improved stability of SSZ-13 by Na co-cations is mainly featured in the protection for framework Al sites.
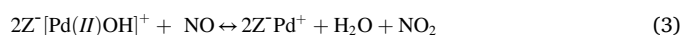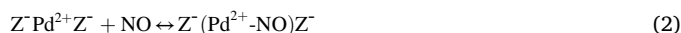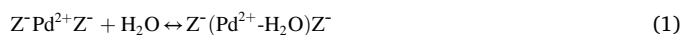
4.2. Enhanced activity promoted by Na co-cations

The NO_x adsorption activity is dependent on the isolated Pd ions at the ionic exchange sites of zeolites. The analysis of ^{27}Al MAS NMR spectra suggests that the aged Pd/Na-13 samples possess more framework Al sites that are beneficial to stabilizing Pd ions. NO-DRIFTS results signify that the Pd^{2+} cations preferentially coordinated with two Al pairing sites ($Z^-Pd^{2+}Z^-$) are dominant in aged Pd/Na-13, while Pd^{2+} coordinated with one isolated Al site ($Z^-[Pd(II)OH]^+$) is the main Pd species in Pd/NH$_4$-13 owing to the partial leaching of framework Al sites after HTA treatment (Fig. 7). The different distribution of Pd active sites in aged Pd/Na-13 and Pd/NH$_4$-13 lead to the distinct performance of NO_x adsorption/desorption. In Section 3.3, the aged Pd/Na-13 sample, e.g., Pd/Na-13–750A, shows the additional NO_x adsorption at above 100 °C, which further enhances NO_x storage capacity in the whole PNA process (Fig. 10). It reported that the second uptake was attributed to Pd ions after decomposition of Pd-hydrate ions in as-prepared Pd/SSZ-13 during the temperature ramp [20,37,42,45]. In order to analyze the additional NO_x uptake definitely, the NO_x adsorption experiments of the Pd-free NH$_4$-SSZ-13 and Na-SSZ-13 were conducted. As shown in Fig. S10, both NH$_4$-SSZ-13 and Na-SSZ-13 show negligible NO adsorption. It signifies the NO_x uptake is completely attributed to the Pd sites rather than Brønsted acid sites in the presence of water, which is line with the observation of Gupta et al. [42].

As shown in Eq. (1) which shows the release of H_2O from $Z^-Pd^{2+}Z^-$ sites, we propose that NO_x adsorbs at the $Z^-Pd^{2+}Z^-$ sites that are Pd ions coordinated with two Al sites, rather than $Z^-[Pd(II)OH]^+$. Our study shows that, unlike the results reported by Gupta et al. [42] that found NO uptake occurs on $Z^-[Pd(II)OH]^+$ and the release of H_2O from $Z^-[Pd(II)OH]^+$ frees up sites for additional NO binding, the second NO uptake (at around 170 °C) is assigned to the NO adsorption on $Z^-Pd^{2+}Z^-$ sites. Zhao et al. [21] discussed the reason that the $Z^-[Pd(II)OH]^+$ sites exhibit high NO adsorption capacity at 100 °C which shows no additional NO adsorption at above 100 °C. They pointed out that the in-situ DRIFTS measurements were performed in the dry feed, the final state of Pd in the dehydrated samples could be different from that NO_x uptake process in the presence of water [21]. In previous studies, the in-situ NO-DRIFTS experiments are performed with the presence of H_2O in the feed [16,43,45,46]. As reported, the NO adsorption on $Z^-Pd^{2+}Z^-$ is inhibited significantly by the presence of H_2O, whereas the NO adsorption on $[Pd(II)OH]^+$ is maintained obviously. The formation of $[Z^-(Pd^{2+}-H_2O)Z^-]$ has been confirmed by experiment and computational modeling [45,46]. In addition, based on our investigation (Fig. 7b), the distribution of Pd ions in Pd/NH$_4$-13–750A is mainly $[Pd(II)OH]^+$. However, there are no additional adsorption peaks in the NO_x curves at above 100 °C (Fig. 9b). It indicates that $[Pd(II)OH]^+$ exhibits the most NO adsorption capacity at 100 °C rather than in the range of 100 – 200 °C, which is in line with the observation of Zhao et el. [21]. Therefore, we infer that it is the $Z^-Pd^{2+}Z^-$ stabilized by two Al sites leading to the second adsorption of NO, hence increasing the total amount of NO_x adsorption (Fig. 10).

As for the NO_x desorption curves, the number of desorption peaks implies different adsorption sites in Pd/Na-13 and Pd/NH$_4$-13 samples (Fig. 9). For Pd/Na-13–750A, the majority of adsorbed NO_x releases at a maximum temperature of 307 °C, which is attributed to the release of Pd^{2+}-NO (Eq. 2) [29]. The desorption temperature is suitable for subsequent NO_x catalytic abatement by NH$_3$-SCR catalysts. While the Pd/NH$_4$-13–750A shows two NO_x desorption peaks at ~175 and ~416 °C, respectively. They are not suitable desorption temperatures for NO_x release. The Eq. (2) and Eq. (4) represent the presence of two kinds of Pd sites, which is indicated by the two NO_x desorption peaks in NO_x storage and release curves over Pd/Na-13-F and Pd/NH$_4$-13-F. As reported, the desorption at low temperature is related to the release of Pd^{2+}-NO (Eq. 2), while the desorption at high temperature corresponds

to the release of Pd^+-NO (Eq. 4) which is ascribed to the reduction of $[Pd(II)OH]^+$ by NO (Eq. 3) [47,48]. The Eq. (3) shows the reduction of two $[Pd(II)OH]^+$ and the generation of NO_2 during NO uptake, thus forming the Pd^+-NO complex which is detected by NO-DRIFTS experiment in our study. Additionally, the formation of NO_2 is observed by NO_x adsorption and desorption curves of aged Pd/NH$_4$-13 in Fig. 9d, while the aged Pd/Na-13 samples exhibit no peaks assigned to NO_2 during NO storage (Fig. 9c) for minor $[Pd(II)OH]^+$. Note that the aged Pd/NH$_4$-13 shows much more NO_x desorption at high temperature than Pd/NH$_4$-13-F, which is ascribed to the much higher content of $[Pd(II)OH]^+$ [49,50]. Possible storage/release processes are depicted as follows (Z^- represents $[Si-O-Al]^-$) [29,45–48]:

$$Z^-Pd^{2+}Z^- + H_2O \leftrightarrow Z^-(Pd^{2+}-H_2O)Z^- \tag{1}$$

$$Z^-Pd^{2+}Z^- + NO \leftrightarrow Z^-(Pd^{2+}-NO)Z^- \tag{2}$$

$$2Z^-[Pd(II)OH]^+ + NO \leftrightarrow 2Z^-Pd^+ + H_2O + NO_2 \tag{3}$$

$$Z^-Pd^+ + NO \leftrightarrow Z^-Pd^+\text{-}NO \tag{4}$$

The enhancement of activity is directly correlated to the aging temperature. In our study, the enhancement by Na co-cations is observed at relatively moderate temperature (≤800 °C). It shows that the adsorption activity of Pd/Na-13 is inhibited by HTA treatment at a high temperature (i.e., 850 °C). HAADF-STEM image (Fig. 4d) and H$_2$-TPR results (Fig. 6a) show that large metallic Pd particles are present in Pd/Na-13–850A. Likewise, the aggregated Na are observed in Fig. S6. Compared with HTA samples at temperatures below 800 °C, the adsorption peaks of Pd ions in Pd/Na-13–850A decrease significantly, as evidenced by NO- and CO-DRIFTS results (Figs. 7a and 8a). In combination with the stable coordination environment of Al in Pd/Na-13–850A in Fig. 2a, the loss of Pd ions cannot be attributed to dealumination. The decrease of adsorption capacity could be due to the possibility that the Na co-cations fall off from the Brønsted acid sites and poison the Pd active sites, i.e., the Pd/Na-13–850A is poisoned by the excess Na, leading the formation of PdO and then the aggregated PdO decomposes into metallic Pd during hydrothermal aging treatment at 850 °C for 12 h. It should be noted that the as-prepared Na-SSZ-13 contains Na content of ~2.8 wt% without further ionic exchange. In a previous study of Xie et al. [23], the Cu$_{3.9}$Na$_{0.8}$-SSZ-13 (Si/Al$_2$ =10.4) contained Na content of ~0.8 wt% shows the optimal activity and hydrothermal stability for NH$_3$-SCR. Chen et al. [34] reported that the existence of 0.77 wt% Na promotes the long-term stability of Cu/SSZ-13 (Si/Al=14). In addition, the agglomeration of CuO$_x$ cluster was observed by Zhao et al. [25] in Cu-Na-SSZ-13 (Si/Al=4) with the increasing of Na content. Therefore, we suggest that the content of Na co-cations should be tuned with optimal Na incorporation to cope with more stringent hydrothermal aging in view of practical application. Both the amount of Na and the activation temperature would be comprehensively investigated in our following work.

4.3. The proposed mechanism of Na co-cations

The influence of Na co-cations in Pd/SSZ-13 for low-temperature NO adsorption is depicted in Fig. 11. As reported by Zhao et al. [21], HTA treatment at harsh temperature caused the dealumination of zeolite that led to the sintering of Pd and the deactivation of Pd/SSZ-13. The degradation phenomenon after HTA treatment is also detected over Pd/NH$_4$-13–850A sample in this study. As shown in Fig. 11a, the hydrolysis of the zeolite framework is induced by the attack of water to Si-O(H)-Al bonds in SSZ-13, leading to the formation of detached Al(OH)$_3$ as evidenced by the ^{27}Al MAS NMR results (Fig. 2). It is noted that the further hydrolysis of Pd species is also responsible for the PdO agglomeration. As for Pd/Na-13, the Na co-cations protect the structure by occupying a portion of BAS (Fig. S4), thus helping to mitigate
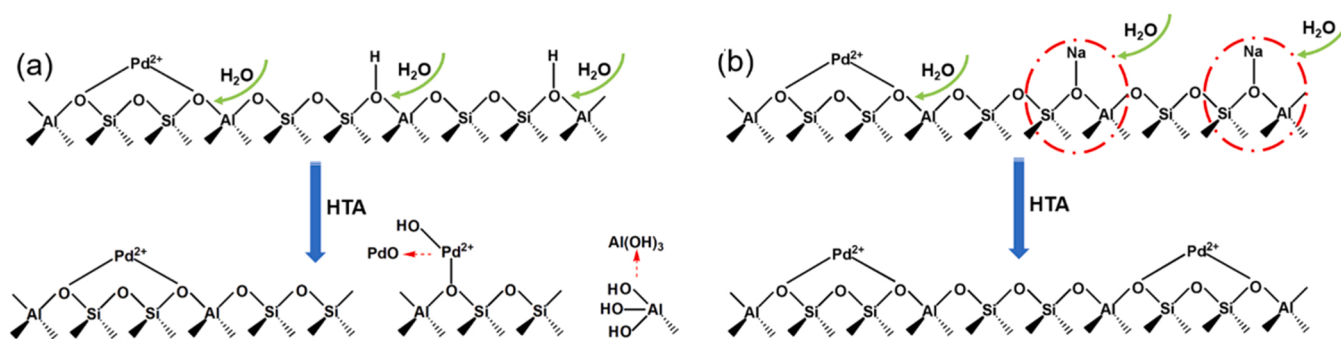
Fig. 11. Hydrolysis process of Pd/NH$_4$-13 (a) and the proposed protection mechanism of residual Na co-cations in Pd/Na-13 during hydrolysis process (b).

hydrolysis of the zeolite during HTA treatment [24,26]. In other words, the Pd/Na-13 after HTA treatment can preserve more paired Al sites. For Pd/Na-13 (Fig. 11b), the Pd cations preferentially combine with two Al paring sites [46]. The Na co-cations are located at the BAS of the SSZ-13 as demonstrated by Chen et al. [26]. During hydrothermal aging treatment, the Na co-cations play a protective role for Si-O(H)-Al. Furthermore, the release of BAS provides ion-exchange sites for Pd ions during HTA treatment. As a result, more Pd ions are stabilized by paired Al sites in hydrothermally aged Pd/Na-13 samples.

5. Conclusion

In summary, Pd/Na-13 and Pd/NH$_4$-13 with comparable Pd contents were prepared and then hydrothermally aged at 750, 800, and 850 °C for low-temperature NO adsorption. During HTA treatment, Na co-cations can stabilize Brønsted acid sites and leave ion-exchange sites for Pd cations. The presence of Na co-cations leads to enhanced stability and activity after activation by mild hydrothermal aging treatment (≤800 °C).

Textural properties of the Pd/Na-13 samples are well maintained after HTA treatment up to 850 °C, while the aged Pd/NH$_4$-13 samples suffer from severe dealumination. The hydrothermally aged Pd/Na-13 and Pd/NH$_4$-13 materials exhibit different distributions of active Pd ions. After HTA treatment, Pd/Na-13 contains much more Pd^{2+} sites, while Pd/NH$_4$-13 has more [Pd(II)OH]$^+$ sites. As expected, the Pd/Na-13–750A shows maximum adsorption capacity. Moreover, the aged Pd/Na-13 exhibit remarkably improved NO adsorption ability at the temperature range of 100 – 200 °C, compared with aged Pd/NH$_4$-13. In addition, the Pd/Na-13 samples after HTA treatment show satisfactory NO$_x$ desorption behavior, i.e., the majority of NO$_x$ desorbed at below 350 °C.

Our study reveals that the stability and activity of hydrothermally aged Pd/SSZ-13 can be highly promoted by Na co-cations. Thus, it is necessary to remain part of the residual Na ions in Pd/SSZ-13 for PNA process. The present work provides useful guidance for further facilitating the hydrothermal stability and activity of the Pd/SSZ-13 in the practical PNA process.

CRediT authorship contribution statement

Dan Li: Investigation, Writing – original draft. **Guoju Yang:** Writing – review & editing. **Mengyang Chen:** Investigation. **Lei Pang:** Supervision. **Yanbing Guo:** Resources. **Jihong Yu:** Resources, Writing – review & editing. **Tao Li:** Funding acquisition, Writing – review & editing.

Declaration of Competing Interest

The authors declare that they have no known competing financial interests or personal relationships that could have appeared to influence the work reported in this paper.

Acknowledgments

Appendix A. Supporting information

Supplementary data associated with this article can be found in the online version at doi:10.1016/j.apcatb.2022.121266.

References

[1] F. Gholami, M. Tomas, Z. Gholami, M. Vakili, Technologies for the nitrogen oxides reduction from flue gas: a review, Sci. Total. Environ. 714 (2020) 136712.

[2] L.P. Han, S.X. Cai, M. Gao, J.Y. Hasegawa, P.L. Wang, J.P. Zhang, L.Y. Shi, D. S. Zhang, Selective catalytic reduction of NO$_x$ with NH$_3$ by using novel catalysts: state of the art and future prospects, Chem. Rev. 119 (2019) 10916–10976.

[3] C. Fan, Z. Chen, L. Pang, S.J. Ming, X.F. Zhang, K.B. Alberta, P. Liu, H.P. Chen, T. Li, The influence of Si/Al ratio on the catalytic property and hydrothermal stability of Cu-SSZ-13 catalysts for NH$_3$-SCR, Appl. Catal. A Gen. 550 (2018) 256–265.

[4] S.T. Zhang, S.J. Ming, L. Guo, C. Bian, Y. Meng, Q. Liu, Y.H. Dong, J.J. Bi, D. Li, Q. Wu, K.W. Qin, Z. Chen, L. Pang, W.Q. Cai, T. Li, Controlled synthesis of Cu-based SAPO-18/34 intergrowth zeolites for selective catalytic reduction of NOx by ammonia, J. Hazard. Mater. 414 (2021), 125543.

[5] Z. Chen, Q. Liu, L. Guo, S.T. Zhang, L. Pang, Y. Guo, T. Li, The promoting mechanism of in situ Zr doping on the hydrothermal stability of Fe-SSZ-13 catalyst for NH$_3$-SCR reaction, Appl. Catal. B Environ. 286 (2021), 119816.

[6] J. Lee, J.R. Theis, E.A. Kyriakidou, Vehicle emissions trapping materials: successes, challenges, and the path forward, Appl. Catal. B Environ. 243 (2019) 397–414.

[7] G.H. Wu, B.B. Chen, Z.F. Bai, Q. Zhao, Z.H. Wang, C.S. Song, X.W. Guo, C. Shi, Cobalt oxide with flake-like morphology as efficient passive NO$_x$ adsorber, Catal. Commun. 149 (2021), 106203.

[8] K. Khivantsev, N.R. Jaegers, L. Kovarik, J.C. Hanson, F.(Feng) Tao, Y. Tang, X. Zhang, I.Z. Koleva, H.A. Aleksandrov, G.N. Vayssilov, Y. Wang, F. Gao, J. Szanyi, Achieving atomic dispersion of highly loaded transition metals in small-pore zeolite SSZ-13: high-capacity and high-efficiency low-temperature CO and passive NO$_x$ adsorbers, Angew. Chem. Int. Ed. 57 (2018) 16672–16677.

[9] Y.T. Gu, W.S. Epling, Passive NO$_x$ adsorber: an overview of catalyst performance and reaction chemistry, Appl. Catal. A Gen. 570 (2019) 1–14.

[10] D.W. Yao, R.F. Ilmasani, J.C. Wurzenberger, T. Glatz, J. Han, A.Y. Wang, D. Creaser, L. Olsson, Kinetic modeling of CO assisted passive NO$_x$ adsorption on Pd/SSZ-13, Chem. Eng. J. 428 (2022), 132459.

[11] J.A. Cole, System for reducing NOx from mobile source engine exhaust, U.S. Patent 5,656,244 A, (1997).

[12] M. Moliner, A. Corma, From metal-supported oxides to well-defined metal site zeolites: the next generation of passive NO$_x$ adsorbers for low-temperature control of emissions from diesel engines, React. Chem. Eng. 4 (2019) 223–234.

[13] K. Khivantsev, X.Y. Wei, L. Kovarik, N.R. Jaegers, E.D. Walter, P. Tran, Y. Wang, J. Szanyi, Palladium/ferrierite versus palladium/SSZ-13 passive NO$_x$ adsorbers: adsorbate-controlled location of atomically dispersed palladium(II) in ferrierite determines high activity and stability, Angew. Chem. Int. Ed. 60 (2021) 2–9.

[14] Y.Y. Ji, S.L. Bai, M. Crocker, Al$_2$O$_3$-based passive NO$_x$ adsorbers for low temperature applications, Appl. Catal. B Environ. 170–171 (2015) 283–292.

[15] Y.Y. Ji, D.Y. Xu, S.L. Bai, U. Graham, M. Crocker, B.B. Chen, C. Shi, D. Harris, D. Scapens, J. Darab, Pt- and Pd-promoted CeO₂-ZrO₂ for passive NOₓ adsorber applications, Ind. Eng. Chem. Res. 56 (2017) 111–125.

[16] H.-Y. Chen, J.E. Collier, D.X. Liu, L. Mantarosie, D. Durán-Martín, V. Novák, R. R. Rajaram, D. Thompsett, Low temperature NO storage of zeolite supported Pd for low temperature diesel engine emission control, Catal. Lett. 146 (2016) 1706–1711.

[17] J. Lee, Y. Ryou, S. Hwang, Y. Kim, S.J. Cho, H. Lee, C.H. Kim, D.H. Kim, Comparative study of the mobility of Pd species in SSZ-13 and ZSM-5, and its implication for their activity as passive NOₓ adsorbers (PNAs) after hydro-thermal aging, Catal. Sci. Technol. 9 (2019) 163–173.

[18] K. Khivantsev, N.R. Jaegers, L. Kovarik, J.Z. Hu, F. Gao, Y. Wang, J. Szanyi, Palladium/zeolite low temperature passive NOₓ adsorbers (PNA): structure-adsorption property relationships for hydrothermally aged PNA materials, Emiss. Control Sci. Technol. 6 (2020) 126–138.

[19] Y. Ryou, J. Lee, S.J. Cho, H. Lee, C.H. Kim, D.H. Kim, Activation of Pd/SSZ-13 catalyst by hydrothermal aging treatment in passive NO adsorption performance at low temperature for cold start application, Appl. Catal. B Environ. 212 (2017) 140–149.

[20] Y.L. Shan, Y. Sun, Y.B. Li, X.Y. Shi, W.P. Shan, Y.B. Yu, H. He, Passive NO adsorption on hydrothermally aged Pd-based small-pore zeolites, Top. Catal. 63 (2020) 944–953.

[21] H.W. Zhao, X.Y. Chen, A. Bhat, Y.D. Li, J.W. Schwank, Insight into hydrothermal aging effect on deactivation of Pd/SSZ-13 as low-temperature NO adsorption catalyst: effect of dealumination and Pd mobility, Appl. Catal. B Environ. 286 (2021) 119874.

[22] R. Simancas, A. Chokkalingam, S.P. Elangovan, Z.D. Liu, T. Sano, K. Iyoki, T. Wakihara, T. Okubo, Recent progress in the improvement of hydrothermal stability of zeolites, Chem. Sci. 12 (2021) 7677–7695.

[23] L.J. Xie, F.D. Liu, X.Y. Shi, F.S. Xiao, H. He, Effects of post-treatment method and Na co-cation on the hydrothermal stability of Cu-SSZ-13 catalyst for the selective catalytic reduction of NO with NH₃, Appl. Catal. B Environ. 179 (2015) 206–212.

[24] F. Gao, Y.L. Wang, N.M. Washton, M. Kollár, J. Szanyi, C.H.F. Peden, Effects of alkali and alkaline earth cocations on the activity and hydrothermal stability of Cu/SSZ-13 NH₃-SCR catalysts, ACS Catal. 5 (2015) 6780–6791.

[25] Z.C. Zhao, R. Yu, R.R. Zhao, C. Shi, H. Gies, F.S. Xiao, D. De Vos, T. Yokoi, X. H. Bao, U. Kolb, M. Feyen, R. McGuire, S. Maurer, A. Moini, U. Müller, W. Zhang, Cu-exchanged Al-rich SSZ-13 zeolite from organotemplate-free synthesis as NH₃-SCR catalyst: effects of Na⁺ ions on the activity and hydrothermal stability, Appl. Catal. B Environ. 217 (2017) 421–428.

[26] Z.X. Chen, X.G. Tan, J. Wang, C. Wang, J.Q. Wang, W. Li, M.Q. Shen, Why does there have to be a residual Na ion as a co-cation on Cu/SSZ-13? Catal. Sci. Technol. 10 (2020) 6319–6329.

[27] H.W. Zhao, Y.N. Zhao, M.K. Liu, X.H. Li, Y.H. Ma, X. Yong, H. Chen, Y.D. Li, Phosphorus modification to improve the hydrothermal stability of a Cu-SSZ-13 catalyst for selective reduction of NOₓ with NH₃, Appl. Catal. B Environ. 252 (2019) 230–239.

[28] Y.R. Cui, Y.L. Wang, E.D. Walter, J. Szanyi, Y. Wang, F. Gao, Influences of Na⁺ co-cation on the structure and performance of Cu/SSZ-13 selective catalytic reduction catalysts, Catal. Today 339 (2020) 233–240.

[29] Y. Ryou, J. Lee, H. Lee, C.H. Kim, D.H. Kim, Effect of various activation conditions on the low temperature NO adsorption performance of Pd/SSZ-13 passive NOₓ adsorber, Catal. Today 320 (2019) 175–180.

[30] K. Khivantsev, N.R. Jaegers, L. Kovarik, M. Wang, J.Z. Hu, Y. Wang, M. A. Derewinski, J. Szanyi, The superior hydrothermal stability of Pd/SSZ-39 in low temperature passive NOₓ adsorption (PNA) and methane combustion, Appl. Catal. B Environ. 280 (2021) 119449.

[31] A.Y. Wang, K. Lindgren, M.Q. Di, D. Bernin, P.-A. Carlsson, M. Thuvander, L. Olsson, Insight into hydrothermal aging effect on Pd sites over Pd/LTA and Pd/SSZ-13 as PNA and CO oxidation monolith catalysts, Appl. Catal. B Environ. 278 (2020), 119315.

[32] Y.L. Shan, W.P. Shan, X.Y. Shi, J.P. Du, Y.B. Yu, H. He, A comparative study of the activity and hydrothermal stability of Al-rich Cu-SSZ-39 and Cu-SSZ-13, Appl. Catal. B Environ. 264 (2020), 118511.

[33] O. Mihai, L. Trandafilović, T. Wentworth, F.F. Torres, L. Olsson, The effect of Si/Al ratio for Pd/BEA and Pd/SSZ-13 used as passive NOₓ adsorbers, Top. Catal. 61 (2018) 2007–2020.

[34] Z.X. Chen, J. Wang, J.M. Wang, C. Wang, J.Q. Wang, W. Li, M.Q. Shen, Disparate essences of residual, ion-exchanged, and impregnated Na ions on topology structure for Cu/SSZ-13 NH₃ selective catalytic reduction catalysts, Ind. Eng. Chem. Res. 58 (2019) 20610–20619.

[35] Y.Y. Ji, S.L. Bai, D.Y. Xu, D.L. Qian, Z.L. Wu, Y. Song, R. Pace, M. Crocker, K. Wilson, A. Lee, D. Harris, D. Scapens, Pd-promoted WO₃-ZrO₂ for low temperature NOₓ storage, Appl. Catal. B Environ. 264 (2020), 118499.

[36] D.D. Chen, H.R. Lei, W.W. Xiong, Y. Li, X. Ji, J.Y. Yang, B.V. Peng, M.L. Fu, P. R. Chen, D.Q. Ye, Unravelling phosphorus-induced deactivation of Pd-SSZ-13 for passive NOₓ adsorption and CO oxidation, ACS Catal. 11 (2021) 13891–13901.

[37] J. Lee, J. Kim, Y. Kim, S. Hwang, H. Lee, C.H. Kim, D.H. Kim, Improving NOₓ storage and CO oxidation abilities of Pd/SSZ-13 by increasing its hydrophobicity, Appl. Catal. B Environ. 277 (2020), 119190.

[38] Z.X. Chen, M.D. Wang, J. Wang, C. Wang, J.Q. Wang, W. Li, M.Q. Shen, Investigation of crystal size effect on the NOₓ storage performance of Pd/SSZ-13 passive NOₓ adsorbers, Appl. Catal. B Environ. 291 (2021), 120026.

[39] M. Ambast, K. Karinshak, B.M.M. Rahman, L.C. Grabow, M.P. Harold, Passive NOₓ adsorption on Pd/H-ZSM-5: experiments and modeling, Appl. Catal. B Environ. 269 (2020), 118802.

[40] Y. Kim, S. Hwang, J. Lee, Y. Ryou, H. Lee, C.H. Kim, D.H. Kim, Comparison of NOₓ adsorption/desorption behaviors over Pd/CeO₂ and Pd/SSZ-13 as passive NOₓ adsorbers for cold start application, Emiss. Control Sci. Technol. 5 (2019) 172–182.

[41] J. Lee, Y. Ryou, S.J. Cho, H. Lee, C.H. Kim, D.H. Kim, Investigation of the active sites and optimum Pd/Al of Pd/ZSM-5 passive NO adsorbers for the cold-start application: evidence of isolated-Pd species obtained after a high-temperature thermal treatment, Appl. Catal. B Environ. 226 (2018) 71–82.

[42] A. Gupta, S.B. Kang, M.P. Harold, NOₓ uptake and release on Pd/SSZ-13: impact of feed composition and temperature, Catal. Today 360 (2021) 411–425.

[43] E.A. Kyriakidou, J. Lee, J. Choi, M. Lance, T.J. Toops, A comparative study of silver- and palladium-exchanged zeolites in propylene and nitrogen oxide adsorption and desorption for cold-start applications, Catal. Today 360 (2021) 220–233.

[44] S. Yasumura, H. Ide, T. Ueda, Y. Jing, C. Liu, K. Kon, T. Toyao, Z. Maeno, K. Shimizu, Transformation of bulk Pd to Pd cations in small-pore CHA zeolites facilitated by NO, JACS Au 1 (2021) 201–211.

[45] P. Kunal, T.J. Toops, M.K. Kidder, M.J. Lance, Deactivation trends of Pd/SSZ-13 under the simultaneous presence of NO, CO, hydrocarbons and water for passive NOₓ adsorption, Appl. Catal. B Environ. 299 (2021), 120591.

[46] K. Mandal, Y. Gu, K.S. Westendorff, S. Li, J.A. Pihl, L.C. Grabow, W.S. Epling, C. Paolucci, Condition-dependent Pd speciation and NO adsorption in Pd/Zeolites, ACS Catal. 10 (2020) 12801–12818.

[47] D.H. Mei, F. Gao, J. Szanyi, Y. Wang, Mechanistic insight into the passive NOₓ adsorption in the highly dispersed Pd/HBEA zeolite, Appl. Catal. A Gen. 569 (2019) 181–189.

[48] C. Liu, J. Wang, Z.X. Chen, J.Q. Wang, M.Q. Shen, Improvement of NOₓ uptake/release over Pd/Beta by propylene: shielding effect of intermediates on adsorbed NOₓ species, Phys. Chem. Chem. Phys. 23 (2021) 5261–5269.

[49] H.W. Zhao, X.Y. Chen, A. Bhat, Y.D. Li, J.W. Schwank, Understanding the chemistry during the preparation of Pd/SSZ-13 for the low-temperature NO adsorption: the role of NH₄-SSZ-13 support, Appl. Catal. B Environ. 282 (2021), 119611.

[50] M. Ambast, A. Gupta, B.M.M. Rahman, L.C. Grabow, M.P. Harold, NOₓ adsorption with CO and C₂H₄ on Pd/SSZ-13: experiments and modeling, Appl. Catal. B Environ. 286 (2021), 119871.